Time-dependent crustal accretion on the Southeast Indian Ridge revealed by Malaysia Airlines flight MH370 search

Ross Parnell-Turner[1], Shi J. Sim[2], Jean-Arthur Olive[3]

[1]Institute of Geophysics and Planetary Physics, Scripps Institution of Oceanography, University of California, San Diego, CA, USA

[2] Department of Terrestrial Magnetism, Carnegie Institution for Science, Washington, 5241 Broad Branch Rd, Washington DC, USA

[3]Laboratoire de Géologie, Ecole Normale Supérieure / CNRS UMR 8538, PSL Research University, 24 rue Lhomond, 75005, Paris, France

Corresponding author: Ross Parnell-Turner (rparnellturner@ucsd.edu)

Key Points:

- Multibeam bathymetric data from MH370 search reveal off-axis crustal structure of Southeast Indian Ridge.
- Crustal accretion fluctuates at a characteristic time scale of 300–400 kyr, with no evidence for periodicity at glacial cycle intervals.
- Crustal accretion variability could be explained by the combined effects of melt-rich porosity waves and mantle heterogeneities.

Abstract

Our understanding of oceanic crustal formation is mostly limited to observations of young crust formed in the past several million years, due to the thick sediments on older crust, and the remote location of many spreading centers. Here we use 40 m-resolution bathymetric data collected over hundreds of square kilometers during the search for Malaysia Airlines Flight 370 on the flank of the Southeast Indian Ridge, which provides a record of crustal accretion from 11–23 Ma. Spectra calculated from the data show a characteristic timescale of 300–400 kyr, and no evidence for periodicity coinciding with glacial cycles. This characteristic timescale could be explained by fluctuations in melt supply and the amount of faulting, leading to variations in crustal thickness. We show that this timescale of variation is consistent with porosity waves observed in a two-phase flow model, which persist over millions of years.

Plain Language Summary

A 12 million year long record of crustal formation is contained within the seafloor mapping data collected during the search for Malaysia Airlines Flight 370, at a resolution that is 15 times higher than previous maps. These data illuminate the structure of a vast area of crust formed on the Southeast Indian Ridge, and show that crustal production, rather than being a constant process, has varied in cycles that last hundreds of thousands of years. This pattern can be explained by the varying amount of molten rock that rises from deep in Earth's mantle, arriving in episodic waves. This behavior could be a general feature of mid-ocean ridges spreading at similar rates, which has not been previously recognized due to a lack of available data.

1. Introduction

Despite oceanic crust covering two-thirds of Earth's surface, the processes that control its formation remain hotly debated (Bonatti et al., 2003; Brunelli et al., 2018; Crowley et al., 2015; Tolstoy, 2015). There is general agreement that mantle upwelling at mid-ocean ridges leads to decompression and partial melting, generating magma that moves to the ridge axis and freezes to form new oceanic crust. While observations along mid-ocean ridge crests have shown that this process varies spatially between and within spreading segments (e.g. Carbotte et al., 2013; Dalton et al., 2014; Maia et al., 2007), little is known about how crustal formation varies through time. Temporal variations in the temperature and composition at the mid-ocean ridge are recorded within the crust along plate-spreading flowlines. This temporal record is, however, usually obscured off-axis by thick sediment, meaning that crustal structure cannot be resolved by shipboard bathymetric data. Seismic reflection techniques can be used to image tectonic structure beneath the sediment, however coverage is sparse, and mostly confined to continental margins, or within a few kilometers of the ridge axis (e.g. Canales et al., 2000).

Here, we tackle this problem using multibeam bathymetric data collected during the multinational search for aircraft wreckage following the disappearance of Malaysia Airlines Flight 370 (MH370; Fig.1). A subset of these data extends over an area of 110,000 km^2 northeast of the intermediate-spreading Southeast Indian Ridge (SEIR; full rate 70.8 mm yr^{-1}; Royer & Schlich, 1988), providing data along flowlines up to 450 km long and covering crust that is 11–23 million years old. Sedimentation rates in this region over the past 28 Myr are thought to be only 0.4–5.5 mm kyr^{-1} (e.g. Ocean Drilling Program Site 752A; Coffin et al., 2000; Rea et al., 1990), meaning that the sediments are sufficiently thin that the tectono-magmatic fabric of the seafloor can be clearly imaged by multibeam bathymetric sonar.

The most robust constraints to date on the timescale of crustal accretion come from the Vema transform region in the north Atlantic ocean, where a ~26 Myr-long record of accretion at the slow-spreading Mid-Atlantic Ridge (MAR; full rate ~25 mm yr^{-1}) is exposed along a 300 km-long flow line (Bonatti et al., 2003, 2005; Cipriani et al., 2009). Synchronous, 3–4 Myr-long variations in the composition of mantle-derived ultramafic rocks and in the residual mantle Bouguer anomaly (RMBA; a proxy for crustal thickness) are evident at the Vema transform zone (Bonatti et al., 2003; Brunelli et al.,

2006). These short wavelength oscillations could be explained as buoyancy-driven thermal pulses at the base of the melting column (Bonatti et al., 2003), which may also be modulated by the presence of a pyroxenite bearing heterogeneous melt source (Brunelli et al., 2018).

Inferred from gravity data alone, similar periodicity in crustal accretion of 2–5 Myr has been suggested on the MAR between the Atlantis and Kane fracture zones (Pariso & Sempéré, 1995; Tucholke et al., 1997). Horizontal variations in seismic *P*-wave velocity south of the Kane fracture zone (FZ) suggest that two adjacent episodes of magmatic and amagmatic spreading could occur in just 400–800 kyr (Canales et al., 2000). This result supports the notion that there is a delicate balance between magma supply and crustal accretion style, however since this single profile is restricted to within 20 km (or ~1.6 Myr) of the ridge axis, it is difficult to apply more generally. Crustal thickness variability on time scales between 100 kyr and 1 Myr were also inferred from a 74-Myr long gravity and bathymetry survey across the Mid-Atlantic Ridge (Shinevar et al., 2019). These authors noted, however, that the thick sediment cover of older abyssal hills could obscure the relationship between seafloor characteristics and crustal geometry.

Fluctuations in mid-ocean ridge magma supply on even shorter time scales (≤100 kyr) have also been proposed on the basis of numerical modeling and spectral analysis of seafloor bathymetry, sparking some controversy. Characteristic distances in the fabric of abyssal hills at the Chile Ridge and at the SEIR have been found to correspond to periods close to those of Milankovitch orbital periodicities (i.e., climatic cycles at periods of 23, 41 and 100 kyr; Crowley et al., 2015; Huybers et al., 2016), suggesting a potential impact of sea level fluctuations on seafloor fabric. At the East Pacific Rise (EPR), 3D multi-channel seismic images suggest crustal thickness variations on timescales of 80–100 kyr, which could be explained by sea level-modulated mantle melting (Boulahanis et al., 2020). This hypothesis has significant and far-reaching implications, including the notion that abyssal hills could provide a record of global sea level fluctuations over millions of years, leading to vigorous debate (e.g. Goff, 2015; Olive et al., 2015, 2016). A comprehensive analysis of abyssal hill statistics tested this notion using data covering crust 0–7 Myr in age from the East Pacific Rise, and 0–2 Myr from the SEIR (Goff et al., 2018). By stacking a large number of bathymetric profiles in the time domain, Goff et al.

(2018) found that abyssal hill topography is random, with no evidence for a coherent climate-driven signal.

The data analyzed here provide a record of crustal accretion at intermediate spreading rates over a period of ~12 Myr, without the complications of amagmatic spreading that influence findings from the MAR (e.g. Bonatti et al., 2003), and far longer than the ~235 kyr-long record from the EPR (Boulahanis et al., 2020). These data span an along-axis distance of ~255 km over two spreading segments, providing a large number of adjacent profiles that are amenable to stacking.

2. Data

Multibeam bathymetric data were collected by hull-mounted sonars on the *MV Fugro Equator*, MV *Fugro Supporter*, and the Chinese naval vessel *Zhu Kezhen* between June 2014 and June 2016, and processed to generate a 40 m × 40 m resolution grid (Smith and Marks, 2014; Picard et al., 2018). Here we analyze a subset of these data located ~120 km northeast of the SEIR, covering an area ~220 x 400 km between the southernmost extent of the search area, and the southwestern edge of faulting and tectonic features associated with the Diamantina trench (Fig. 1). The Geelvinck fracture zone (FZ) separates segment K and segment L of the SEIR (following segment nomenclature from Royer & Schlich, 1988), and is excised from the bathymetric grid for the purposes of analysis.

2.1 Spectral analysis

We use frequency spectra stacked in the time domain in order to increase the amplitude of coherent time-dependent variations with respect to random bathymetric variations (thus enhancing the signal to noise ratio). Our first step is to assign crustal age estimates to the bathymetric data, which requires a crustal age model. Since global age models are constructed at a coarse scale for global tectonic applications (e.g. Müller et al., 2016), there are small errors where zero age crust may not perfectly match the spreading axis (Goff et al., 2018). We compared the global crustal age model of Müller et al., (2016) to multibeam bathymetric and towed sea surface magnetic data over segments K and L of SEIR acquired during cruise BMRG06MV in 1996 (Figure S1; www.marine-geo.org), and found minor (~7 km) discrepancies between the location of

zero-age crust and the spreading axis. The shipboard data include a 10 km-wide bathymetric swath parallel to the ridge axis, and a single magnetic anomaly profile that crosses the axis on segment K, about 40 km northwest of the Geelvinck FZ. We picked the spreading axis based upon the bathymetric peak that corresponds to the center of the Bruhnes-Matuyama magnetic anomaly on the crossing profile (age ~781 ka), and picked the remaining ridge axis in segments K and L based upon bathymetric character alone. In combination with a plate rotation model (Müller et al., 2016), we constructed a smoothed regional crustal age grid for segments K and L using *GPlates* software (Müller et al., 2016, 2018). Based upon the width of the central bathymetric peak at the spreading axis along segments K and L, we estimate a minimum lateral uncertainty of ~500 m, which translates to a temporal resolution of ~0.014 Myr. While there is uncertainty in this age determination, largely due to the sparse magnetic anomaly data available in this remote area, this is offset by our approach of stacking profiles in the frequency domain, hence absolute age constraints are less important.

Bathymetric profiles, spaced 500 m apart, were extracted along plate spreading flowlines, using the trend of the Geelvinck FZ as the most accurate local indicator of the plate motion vector. We excluded areas that show deformation associated with the Geelvinck FZ and the Diamantina trench, areas of volcanism related to the series of SW-NE trending seamounts centered at ~88.6° in segment L, and the oblique features south of the Geelvinck FZ near 89°W (see dashed polygon in Fig. 1a). The resulting set of profiles span a total of 275 km of along-axis distance, with 350 bathymetric profiles for segment K, and 400 profiles for segment L. Bathymetric depth values were sampled from the MH370 search grid at 50 m intervals along each profile, and crustal age assigned from the regional age model, which was then used to convert each profile into a time series (see examples in Fig. 2).

Profiles were de-trended to account for the effects of long-wavelength plate cooling, and spectral analysis carried out with a multitaper approach using seven tapers following the approach described by Crowley et al. (2015). Spectra were stacked together to produce separate power spectral density estimates for segments K and L (Fig. 2). We also tested the effects of applying prewhitening (i.e. taking the time derivative) prior to calculating bathymetric spectra (Fig. S2), following the approach chosen by Crowley et al. (2015) to better identify spectral peaks amidst a red background

continuum. Prewhitening has the net effect of removing the background slope of the spectrum, and bending the spectra down towards zero power, beginning near the corner period and continuing to longer periods. This bending gives rise to an artificial spectral peak near the corner period (Fig. S2), which we do not interpret as a real signal in the data. Hence we do not use these prewhitened spectra for further analysis.

In order to further characterize variations in crustal structure, we calculated the mantle Bouguer anomaly (MBA) over the study survey area, based upon satellite free-air gravity anomaly data (Sandwell et al., 2014). The MBA was obtained by removing the gravitational effects of the water-crust and crust-mantle interfaces from the free-air gravity anomaly using an upward-continuation method assuming a crustal thickness of 6 km, and crustal and mantle densities of 2700 and 3300 kg m^{-3}, respectively (see Figure S3; Parker, 1973). The MBA was combined with a thermal correction to estimate the residual mantle Bouguer anomaly and relative crustal thickness, shown in Fig. S3f. Profiles and corresponding spectra were extracted from the resulting MBA grid (Figs. 2c–f), both with and without prewhitening for comparison (Fig. 2 and Fig S2). We calculated spectrograms as a function of distance from the Geelvinck FZ, by interpolating between adjacent spectra to investigate patterns of crustal accretion within each segment (Fig. S4). No clear difference in spectral power is evident between the two segments, and within each segment, spectrograms reflect the typical power law relation with increasing power up to ~400 kyr.

3.1 Results: timescales of crustal accretion

Spectra obtained from our analysis of bathymetric profiles have a constant (i.e., white) power spectrum at long periods, which transitions to a power-law (fractal) spectrum at shorter periods. The transition between these two behaviors is marked by the change in slope of the spectra equivalent to a corner period, and defines a characteristic scale of morphology (Goff & Arbic, 2010; Goff & Jordan, 1988). This spectral character closely resembles a spectral model (von Kármán, 1948), which has been previously adapted to two dimensions to describe the statistical properties of abyssal hills (Goff et al., 1997; Goff & Arbic, 2010; Goff & Jordan, 1988). Following this approach, we applied a linear fit in log-log space to the short and long period portions of each spectrum

(defined as >100 kyr and < 1 Ma, respectively), and used the intercept between these projected fits to obtain an estimate a corner period of 300–400 kyr (Fig 2).

In order to test the significance of spectral peaks at periods <400 kyr, we approximated a null hypothesis for the power-law portion of the spectra using a linear fit (Fig. 2). We calculated the confidence intervals for this null hypothesis at 2σ (i.e. 95% confidence), and at 4σ. In the null hypothesis, 5% of peaks are expected to fall outside of the 95% confidence bound; hence in order to be significant, we required peaks in the observed spectra to exceed the 4σ bound (Fig. 2). Since no peaks in the observed spectra satisfy this criteria, we cannot reject the null hypothesis, and conclude that minor peaks in the spectra at periods <400 kyr are random fluctuations typically expected in the power law process. Hence we find no evidence for seafloor bathymetric features corresponding to glacial cycles at periods of 23, 41 and 100 kyr.

The observed characteristic timescale of 300–400 kyr is consistent with the hundreds of kyr-long crustal accretion cycles observed along single crustal profiles at the MAR (Canales et al., 2000, Shinevar et al., 2019), but shorter than the ~3 Myr cycles reported by Bonatti et al. (2003). Below this corner period, the shorter period component of the bathymetric spectra (i.e. shorter wavelength and higher frequency, to the right in Figs. 2d and 2e) deviates considerably from the MBA spectra, providing evidence that this short period signal represents the faulted component of bathymetry. Above this corner period, the bathymetric and MBA spectra have similar character, suggestive of a common, long-wavelength process likely to be related to crustal thickness and melt supply.

3.2 Spatial and temporal variations in magmatism

Our spectral approach indicates that seafloor bathymetry contains a record of crustal accretion that is dominantly stochastic, giving rise to seafloor morphology that follows a power-law relationship at periods <400 kyr. We do, however, find some evidence that crustal accretion may vary on characteristic time scales between 300 and ~400 kyr (Fig. 2). To further quantify these patterns in terms of accretion processes, we estimate the proportion of plate spreading accommodated by faulting versus magmatism in space and time. First, we calculated the magnitude and azimuth of steepest slope for each grid node in the bathymetric survey (Fig. 3a). We then extracted slope and azimuth

values along flowlines spaced 500 m apart, and identified extensional normal faults along each bathymetric profile by selecting inward-dipping slopes with magnitude >10° (i.e., dipping towards the ridge axis), with strikes oriented within 20° of the spreading vector. The total horizontal displacement (i.e., sum of individual fault heaves) was calculated over a moving window along each profile (Fig. 3b). The fraction of the window length populated by fault scarps represents the fraction of tectonically-accommodated plate separation (T). The quantity $M = 1 - T$ is classically interpreted as the fraction of plate separation taken up by magmatic accretion at the spreading axis (Buck et al., 2005). In order to explore sensitivity to window length in this estimate, we calculated M using 3, 5 and 10 km-wide windows (Fig. 3b). At 3 km window length, M is more sensitive to local changes in slope, giving locally lower values (~0.8), whereas with a window of 10 km, local minima are ~0.9. Hence we chose a compromise window length of 5 km to account for this potential uncertainty. Adjacent profiles were then combined and interpolated to generate a spatially continuous map of M, plotted in Fig. 3c.

Values of M vary between ~0.85 and 1.0, reflecting the dominantly magmatic accretion style at this intermediate spreading rate (Buck et al., 2005; Howell et al., 2016; Olive et al., 2015). In map view, regions of low M ($0.85 < M < 0.95$) manifest as axis-parallel bands that are less than 10 km wide in the cross-axis direction, extend up to ~120 km along-axis, and are spaced ~20 km apart. This spacing is consistent with the characteristic timescale of 300–400 kyr revealed by our bathymetric spectra, implying accretion cycles on the same time scale. Relative crustal thickness, derived from satellite free-air gravity anomaly, does not show any resolvable dependence upon M (Fig. S5), as similar to findings on the Mid-Atlantic ridge (Shinevar et al., 2019). The limited range in M values here (0.85 to 1.0) may preclude this relationship from being evident. Nonetheless, subtle changes in the balance between melt supply and faulting could explain the observed temporal variations in crustal accretion.

4.1 Discussion

Our bathymetric spectra (Fig. 2) show a continuum pattern, with evidence for a characteristic time period of 300–400 kyr. This range corresponds to wavelengths of ~10 to ~14 km, that is also apparent in MBA spectra, indicating that it could be related to characteristic wavelengths in crustal thickness. We note that the satellite gravity data do

not fully resolve wavelengths less than ~12 km (Sandwell et al., 2014), equivalent to a period of 340 kyr, hence features at such wavelengths are at the limit of resolution. Hence the deviation between the bathymetric and MBA spectra may partly reflect a reduction of sensitivity in the gravity data. The density contrast between the crust and underlying mantle exerts a buoyancy force that can drive flexural-isostatic deflection of young oceanic lithosphere (Watts, 2001). If the wavelength of the deflection exceeds ~100 times the effective elastic thickness (T_e) of near-axis lithosphere, those deflections can be compensated isostatically, which maximizes their topographic expression (Olive et al., 2015). If not isostatically compensated, the effects of plate flexure can strongly hinder or suppress topography because the lithosphere responds more rigidly to shorter-wavelength loads. We used the admittance between bathymetry and gravity data to estimate that the T_e of lithosphere in this region is ~3 km (Supporting Information, and Fig. S6), a value consistent with estimates for young, intermediate-spreading rate lithosphere elsewhere (e.g., Cochran, 1979; Kuo and Forsyth, 1986). Hence, 10–20 km wavelength fluctuations in crustal thickness could be expressed (although partially damped) as fluctuations in bathymetry on the same range of wavelengths, and thus manifest as energy in our bathymetric spectra. By contrast, any rapid (<200 kyr) fluctuation in crustal thickness is much less likely to imprint seafloor topography through flexural-isostatic compensation.

Short-wavelength variations in the bathymetric spectra may instead be due to faulting, which at intermediate-spreading ridges generates abyssal hills that are typically ~2 to 4 km apart, corresponding to characteristic time scales of ~50–150 kyr (Goff et al., 1997). Such structures are evident from the bathymetric maps and profiles (Figs. 1 and 2), and are known to produce complex spectral peaks and their overtones at frequencies of order ~100 kyr (Olive et al., 2016). We propose that the characteristic time scale of 300–400 kyr may partly reflect longer-wavelength changes in the tectonic fabric of the seafloor. Such changes manifest in map view (Fig. 3c) as intermittent high-T (or low-M) regions that are elongated in the along-axis direction, possibly reflecting accretion events that occur synchronously over distances of 20–80 km along the ridge axis (e.g., a sustained drop in the intrusion frequency of dikes that propagate tens of km along the axis). Our estimates of cumulative fault heave (Fig. 3b) suggest that during these periods, M drops to ~0.8–0.9 from a long-term average above ~0.95. In the classical model of

magma intrusion-controlled styles of ridge faulting (Buck et al., 2005; Behn and Ito, 2008), such fluctuations around an average *M* so close to 1 have limited effects on fault characteristics. As a rule of thumb, these models predict that a decrease in *M* from 0.9 to 0.8 at an intermediate spreading ridge would only increase fault spacing (of order ~2–4 km) by ~200 m (Olive et al., 2015). Commensurate increases can be expected for fault heave and throw. Although small, they could cause subtle fluctuations in the tectonic fabric of the seafloor that become apparent in the frequency domain. In particular, the characteristic spacing of the low-*M* bands (Fig. 3c) could account for part of the spectral energy at 300–400 kyr.

This range of periods is consistent with the observation of strong variations in *P*-wave crustal seismic velocities within 15 km of the slow-spreading MAR axis near 23°N (Canales et al, 2000), providing evidence that crustal thickness and thus magmatic input can vary on timescales of hundreds of ka. Our findings are also consistent with characteristic fluctuation periods of 390, 550 and 950 kyr found in bathymetry and gravity over 0–74 Myr-old Atlantic seafloor (Shinevar et al., 2019). However, these cycles are significantly shorter than the ~3–4 Myr oscillations in degree of melting and crustal thickness described at the MAR by Bonatti et al. (2003). Those longer period oscillations have been explained by intermittent buoyant convective mantle upwelling, as a result of non-uniform mantle rheology beneath the ridge axis (Bonatti et al., 2003; Scott & Stevenson, 1989). Numerical models of slow-spreading ridges can explain along-axis spacing of adjacent mantle upwellings as short as 40–70 km, which are driven by a highly viscous shallow region in which the solid is dehydrated by melt extraction (Choblet & Parmentier, 2001). This mechanism is unlikely to generate the 10–20 km wavelength features observed here, since mantle upwelling instabilities are unlikely to be sustained on such fine scales. Our spatial analysis of extensional faulting is consistent with short-term, subtle variations in melt supply, which are likely to drive the observed patterns in seafloor depth.

4.2. Crustal production and magmatic waves

One plausible mechanism for causing subtle, yet rapid variations in *M* is the development of transient, melt-rich porosity waves above the sub-ridge melting triangle, which could modulate melt supply, and hence the thickness of oceanic crust produced at

345 the ridge axis (White et al., 1992). Porosity waves are a fundamental feature of the two-
346 phase flow description of melt transport in the (upper) mantle with non-zero compaction
347 length (McKenzie 1984, Fowler 1985, Scott and Stevenson 1986; Spiegelman 1993a).
348 Buoyant melt accumulates as it moves into a melt-free region, since it is an obstruction of
349 flow due to the viscous resistance of the deformable mantle matrix. As melt accumulates,
350 permeability increases. This accumulation allows melt to segregate faster and thus creates
351 an additional obstruction upstream, encouraging melt to accumulate behind it. This
352 process continues upstream, forming a train of porosity waves of wavelength comparable
353 to the compaction length scale. Recent modeling has shown that porosity waves are likely
354 to persist at slow spreading rates (<20 mm yr^{-1}), hence providing a magmatic mechanism
355 for crustal accretion cycling (Sim et al., 2018).

356 To test the hypothesis that magma supply variability could explain the long-
357 period depth variations observed in the bathymetry on the SEIR, we employ a two-
358 dimensional (2D), two-phase flow model, with half spreading rate of 35 mm yr^{-1} (Fig. 4a;
359 Sim et al., 2018). Further model details and parameters are given in Supporting
360 Information. This two-phase flow setup is based on equations first formulated by
361 McKenzie (1984), Fowler (1985) and Scott and Stevenson (1986), extended to account
362 for conservation of energy (Sim et al., 2018). Crustal thickness over time is calculated
363 using the melt flux at the top of the model domain as a proxy (Fig. 4a). Our objective is
364 to test whether a two-phase flow model can provide a feasible mechanism to explain the
365 hundred of kyr variations in *M* implied by our observations, while not aiming to
366 reproduce specific peaks in the bathymetric spectra. The temporal periodicity in crustal
367 thickness is due to time-dependent melt rich porosity waves in the models (see movie S1
368 in Supporting Information). These melt-rich waves buoyantly propagate from the melting
369 region towards the lithosphere-asthenosphere boundary, where they encounter the cold,
370 strong lithosphere and form a decompaction layer that channels melt towards the ridge
371 axis (Sparks and Parmentier, 1991; Spiegelman, 1993b; Hebert & Montesi, 2010; Keller
372 et al, 2017; Sim et al., 2018).

373 After an initial transient period (lasting ~2 Myr), porosity waves remain
374 persistent in this model, as recognized in similar models at slow spreading rates (Sim et
375 al., 2018). Spectral analysis of the crustal thickness time series shows a corner period on
376 order of 150 kyr, and small spectral peaks periodicities at ~ 300, 150, and 100 kyr (Fig.

4b), consistent with the hundreds of kyr characteristic period observed in bathymetric spectra of the SEIR. Model outputs at double the spatial resolution (and hence increased adaptive temporal resolution) show that the characteristic corner period persists, along with some of the minor spectral peaks (Figs S7 and S8). Wavelength of the porosity waves depends upon compaction length, which is dependent on permeability, bulk viscosity and fluid viscosity, while the phase velocity and amplitude of the waves depend on the initial obstruction (Spiegelman, 1993b). Model asymmetry causes porosity waves to interfere constructively or deconstructively, likely causing variations in periodicity. Although this mechanism can reasonably explain crustal accretion variations that give rise to characteristic morphology on timescales of 100s of kyr, a more extensive modeling effort is required to fully test how the parameters highlighted above affect porosity waves as a magmatic source for varying M .

4.3 Melt channelization

An alternative mechanism to explain crustal accretion cycles could be small-scale mantle heterogeneities, leading to melt channelization as suggested by Katz & Weatherly (2012), and Weatherley & Katz (2012, 2016). Numerical models show that mantle heterogeneities enriched in fusible components can lead to nucleation of magmatic channels (Weatherley & Katz, 2012), along which individual packets of melt may be delivered to the ridge axis on timescales of 25–350 kyr (Weatherley & Katz, 2016). On Iceland, kilometer-scale chemical variability of basalts can be explained by the variable source peridotite fusibility, indicating that variations in source composition and fusibility are present on small length scales (Shorttle & Maclennan, 2011). We suggest that mantle heterogeneities on length scales similar to that observed on Iceland (tens of kilometers), could lead to the presence of more- or less fusible parcels of source material beneath the ridge axis, and in turn generate ephemeral networks of magmatic channels. During periods when more fusible source material is undergoing melting, channelization is favored and melt supply is increased. When less fusible mantle source is within the source region, channelization is inhibited, and melt supply is relatively reduced. Since observed variations in M typically extend along the entire length of segments L and K, this melt channelization mechanism would need to be driven by heterogeneities that are large enough to be sampled along several tens of kilometers of ridge axis at the same

time. If the heterogeneities occur on length-scales shorter than an individual segment, then melt anomalies would generate a patchwork of crustal thickness variations along axis. Since we observe considerable uniformity along-axis, melt channelization alone cannot explain the observed patterns, and therefore we favor the porosity wave mechanism for generating kyr-scale variations in melt supply.

We speculate that if these two possible mechanisms were both acting upon the melt region, any dominant periodicity in crustal production imposed by one may be damped by the effects of the other. Hence their combined effects would be expected to decrease the amplitude of any peaks in the observed bathymetric spectra. The spectra presented here mostly reflect a stochastic continuum, which could be explained by the combined effects of multiple crustal accretion processes that obscure any individual spectral peaks.

Conclusions

Bathymetric data spanning two spreading segments of the intermediate-spreading SEIR show a power law character, with a characteristic corner period of ~300 kyr to 400 kyr. Bathymetric and MBA spectra have similar character only above these periods, supporting the notion that this timescale reflects variations in crustal thickness. The data do not indicate periodicity in crustal accretion at glacial cycle intervals. Spatial variations in fault heave and relative crustal thickness could be explained by relatively subtle changes in the amount of extension accommodated by faulting, which may in turn could be driven by varying magma supply, *M*.

One possible mechanism for such variations in melt supply at slow and intermediate spreading rates are time-varying melt rich porosity waves in the mantle. Our model results demonstrate that this phenomenon can lead to temporal changes in crustal thickness over periods of hundreds of kyr, consistent with the bathymetric observations. Alternatively, small-scale mantle heterogeneity has been shown to lead to melt channelization, which could also generate melt supply variations on similar timescales.

Acknowledgements

We acknowledge the tragic loss of the 239 people on board Malaysia Airlines Flight 370, which led to acquisition of the bathymetric data presented here. We thank J. Goff and M. Maia for their detailed and constructive comments, which greatly improved our work. Multibeam bathymetric data are available from the AusSeabed Marine Data Discovery Interface, hosted by Geoscience Australia (http://marine.ga.gov.au). RPT was supported by National Science Foundation grant OCE-1736547.

References

Behn, M. D., & Ito, G. (2008). Magmatic and tectonic extension at mid-ocean ridges: 1. Controls on fault characteristics. *Geochem. Geophys. Geosyst*, 9(8), doi:10.1029/2008GC001965.

Bonatti, E., Brunelli, D., Buck, W. R., Cipriani, A., Fabretti, P., Ferrante, V., … Ligi, M. (2005). Flexural uplift of a lithospheric slab near the Vema transform (Central Atlantic): Timing and mechanisms. *Earth Planet. Sci. Lett.*, *240*(3–4), 642–655. https://doi.org/10.1016/j.epsl.2005.10.010

Bonatti, E., Ligi, M., Brunelli, D., Cipriani, A., Fabretti, P., Ferrante, V., … Ottolini, L. (2003). Mantle thermal pulses below the Mid-Atlantic Ridge and temporal variations in the formation of oceanic lithosphere. *Nature*, *423*, 499–505. https://doi.org/10.1038/nature01594

Boulahanis, B., Carbotte, S. M., Huybers, P. J., Nedimović, M. R., Aghaei, O., Canales, J. P., & Langmuir, C. H. (2020). Do sea level variations influence mid-ocean ridge magma supply? A test using crustal thickness and bathymetry data from the East Pacific Rise. *Earth and Planetary Science Letters*, *535*, 1–11. https://doi.org/10.1016/j.epsl.2020.116121

Brunelli, D., Cipriani, A., & Bonatti, E. (2018). Thermal effects of pyroxenites on mantle melting below mid-ocean ridges. *Nature Geosci.*, *11*, 520–525. https://doi.org/10.1038/s41561-018-0139-z

Brunelli, D., Seyler, M., Cipriani, A., Ottolini, L., Bonatti, E., Di, D., & Della, S. (2006). Discontinuous Melt Extraction and Weak Refertilization of Mantle Peridotites at the Vema Lithospheric Section (Mid-Atlantic Ridge), *47*(4), 745–771.

https://doi.org/10.1093/petrology/egi092

Buck, W. R., Lavier, L., & Poliakov, A. N. B. (2005). Modes of faulting at mid-ocean ridges. *Nature*, *434*, 719–723. https://doi.org/10.1038/nature03358

Canales, J. P., Collins, J. A., & Detrick, R. S. (2000). Seismic structure across the rift valley of the Mid-Atlantic Ridge at 23°20' (MARK area): Implications for crustal accretion processes at slow spreading ridges. *Journal of Geophyscial Research*, *105*(B12), 28411–28425. https://doi.org/10.1029/2000JB900301

Carbotte, S. M., Marjanovic, M., Carton, H., Mutter, J. C., Canales, J. P., Nedimović, M. R. (2013). Fine-scale segmentation of the crustal magma reservoir beneath the East Pacific Rise. *Nature Geosci.*, *6*(10), 866–870. https://doi.org/10.1038/ngeo1933

Choblet, G., & Parmentier, E. M. (2001). Mantle upwelling and melting beneath slow spreading centers: Effects of variable rheology and melt productivity. *Earth Planet. Sci. Lett.*, *184*(3–4), 589–604. https://doi.org/10.1016/S0012-821X(00)00330-7

Cipriani, A., Bonatti, E., Brunelli, D., & Ligi, M. (2009). 26 million years of mantle upwelling below a segment of the Mid Atlantic Ridge: The Vema Lithospheric Section revisited. *Earth and Planetary Science Letters*, *285*(1–2), 87–95.

Cochran, J.R., 1979. An Analysis of Isostasy in the World's Oceans: 2. Midocean Ridge Crests. *J. Geophys. Res*. 84, 4713–4729.

Coffin, M. F., Frey, F. A., Wallace, P. J., & Shipboard Scientific Party. (2000). *Proc. ODP, Init. Repts.* (Vol. 183). College Station, TX: Ocean Drilling Program.

Crowley, J. W., Katz, R. F., Huybers, P., Langmuir, C. H., & Park, S. (2015). Glacial cycles drive variations in the production of oceanic crust. *Science*, *347*, 1237–1240.

Dalton, C. A., Langmuir, C. H., & Gale, A. (2014). Geophysical and Geochemical Evidence for Deep Temperature Variations Beneath Mid-Ocean Ridges. *Science*, *344*(6179), 80–84. https://doi.org/10.1126/science.1249466

Fowler, A. C. (1985). A mathematical model of magma transport in the asthenosphere. *Geophys. Astrophys. Fluid Dynamics*, 33, 63–96.

Goff, J. A., & Arbic, B. K. (2010). Global prediction of abyssal hill roughness statistics for use in ocean models from digital maps of paleo-spreading rate, paleo-ridge orientation, and sediment thickness. *Ocean Modelling*, *32*(1–2), 36–43. https://doi.org/10.1016/j.ocemod.2009.10.001

Goff, J. A., & Jordan, T. H. (1988). Stochastic Modeling of Seafloor Morphology:

505 Inversion of Sea Beam Data for Second-Order Statistics. *Journal of Geophysical*
506 *Research: Solid Earth*, *93*(B11), 13589–13608.
507 https://doi.org/10.1029/JB093iB11p13589
508 Goff, J. A., Ma, Y., Shah, A., Cochran, J. R., & Sempéré, J.-C. (1997). Stochastic
509 analysis of seafloor morphology on the flank of the Southeast Indian Ridge: The
510 influence of ridge morphology on the formation of abyssal hills. *J. Geophys. Res,*
511 102(B7), 15521. https://doi.org/10.1029/97jb00781
512 Goff, J. A. (2015). Comment on "Glacial cycles drive variations in the production of
513 oceanic crust." *Science*, *349*, 7–9.
514 Goff, J. A., Zahirovic, S., & Muller, R. D. (2018). No Evidence for Milankovitch Cycle
515 Influence on Abyssal Hills at Intermediate, Fast, and Superfast Spreading Rates.
516 *Geophys. Res. Lett.*, *45*, 305–313. https://doi.org/10.1029/2018GL079400
517 Hebert, L. B., & Montési, L. G. J. (2010). Generation of permeability barriers during melt
518 extraction at mid-ocean ridges. *Geochem. Geophys. Geosyst*., 11(12), Q12008.
519 https://doi.org/10.1029/2010GC003270
520 Howell, S. M., Ito, G., Behn, M. D., Martinez, F., Olive, J.-A., & Escartín, J. (2016).
521 Magmatic and tectonic extension at the Chile Ridge: Evidence for mantle controls
522 on ridge segmentation. *Geochem. Geophys. Geosyst*., 17.
523 https://doi.org/doi:10.1002/ 2016GC006380
524 Huybers, P., Langmuir, C., Katz, R. F., Ferguson, D., Proistosescu, C., & Carbotte, S.
525 (2016). Comment on "Sensitivity of seafloor bathymetry to climate-driven
526 fluctuations in mid-ocean ridge magma supply." *Science*, *352*, 34–36.
527 Katz, R. F., & Weatherley, S. M. (2012). Consequences of mantle heterogeneity for melt
528 extraction at mid-ocean ridges. *Earth Planet. Sci. Lett.*, 335–336, 226–237.
529 https://doi.org/10.1016/j.epsl.2012.04.042
530 Keller, T., Katz, R. F., & Hirschmann, M. M. (2017). Volatiles beneath mid-ocean ridges:
531 Deep melting, channelised transport, focusing, and metasomatism. *Earth Planet. Sci.*
532 *Lett.*, 464, 55–68. https://doi.org/10.1016/j.epsl.2017.02.006
533 Kuo, B.-Y., Forsyth, D.F., Parmentier, E.M., 1986. Flexure and thickening of the
534 lithosphere at the East Pacific Rise. Geophys. Res. Lett. 13, 681–684.
535 Maia, M., Goslin, J., & Gente, P. (2007). Evolution of the accretion processes along the
536 Mid-Atlantic Ridge north of the Azores since 5.5 Ma: An insight into the

interactions between the ridge and the plume. *Geochem. Geophys. Geosyst*, *8*(3). https://doi.org/10.1029/2006GC001318

Müller, R. D., Cannon, J., Qin, X., Watson, R. J., & Gurnis, M. (2018). GPlates: Building a Virtual Earth Through DeepTime. *Geochem. Geophys. Geosyst.*, *19*, 2243–2261. https://doi.org/10.1029/2018GC007584

Müller, R. D., Seton, M., Zahirovic, S., Williams, S. E., Matthews, K. J., Wright, N. M., … Cannon, J. (2016). Ocean Basin Evolution and Global-Scale Plate Reorganization Events Since Pangea Breakup. *Annual Review of Earth and Planetary Sciences*, *44*, 107–138. https://doi.org/10.1146/annurev-earth-060115-012211

Olive, J.-A., Behn, M. D., Ito, G., Buck, W. R., Escartín, J., & Howell, S. M. (2016). Response to Comment on "Sensitivity of seafloor bathymetry to climate-driven fluctuations in mid-ocean ridge magma supply." *Science*, *352*(6292), 2–4.

Olive, J.-A., Behn, M. D., Ito, G., Roger Buck, W., Escartín, J., & Howell, S. M. (2015). Sensitivity of seafloor bathymetry to climate-driven fluctuations in mid-ocean ridge magma supply. *Science*, *350*(6258), 310–313.

Pariso, J. E., & Sempéré, J.-C. (1995). Temporal and spatial variations in crustal accretion along the Mid-Atlantic Ridge (29°–31°30' N) over the last 10 m.y.: Implications from a three-dimensional gravity study. *J. Geophys. Res.*, 100(B9), 17,781-17,794.

Parker, R. L. (1973), The rapid calculation of potential anomalies, *Geophys. J. Int.*, 31, 447–455.

Percival, D. B., & Walden, A. T. (1993). *Spectral Analysis for Physical Applications*. Cambridge, UK: Cambridge University Press.

Picard, K., Brooke, B. P., Harris, P. T., Siwabessy, P. J. W., Coffin, M. F., Tran, M., … Sullivan, J. (2018). Malaysia Airlines flight MH370 search data reveal geomorphology and seafloor processes in the remote southeast Indian Ocean. *Marine Geology*, 395, 301–319. doi.org/10.1016/j.margeo.2017.10.014

Rea, D. K., Dehn, J., Driscoll, N. W., Farrell, J. W., Janeck, T. R., Owen, R. M., … Shipboard Scientific Party. (1990). Paleoceanography of the eastern Indian Ocean from ODP Leg 121 drilling on Broken Ridge. *Geol. Soc. Am. Bull.*, *102*, 679–690.

Royer, J.-Y., & Schlich, R. (1988). Southeast Indian Ridge Between the Rodriguez Triple Junction and the Amsterdam and Islands: Detailed Kinematics for the Past 20 m.y. *J.*

569 *Geophys. Res.*, *93*(B11), 13,524-13,550.
570 Sandwell, D. T., Muller, R. D., Smith, W. H. F., Garcia, E., & Francis, R. (2014). New
571 global marine gravity model from CryoSat-2 and Jason-1 reveals buried tectonic
572 structure. *Science*, *346*, 65–67. https://doi.org/10.1126/science.1258213
573 Scott, D. R., & Stevenson, D. J. (1986). Magma Ascent by Porous Flow. *J. Geophys.*
574 *Res.*, 91(B9), 9283–9296.
575 Scott, D. R., & Stevenson, D. J. (1989). A self-consistent model of melting, magma
576 migration and buoyancy-driven circulation beneath mid-ocean ridges. *J. Geophys.*
577 *Res.*, *94*(88), 2973. https://doi.org/10.1029/JB094iB03p02973
578 Shinevar, W., Mark, H., Clerc, F., Codillo, E., Gong, J., Olive, J.-A., Brown, S., Smalls,
579 P., Liao, Y., LeRoux, V. & Behn, M. D. (2019), Causes of oceanic crustal thickness
580 oscillations along a 74-Myr Mid-Atlantic Ridge flow line, *Geochem. Geophys.*
581 *Geosyst*., 20(12), https://doi.org/10.1029/2019GC008711.
582 Shorttle, O., & Maclennan, J. (2011). Compositional trends of Icelandic basalts:
583 Implications for short–length scale lithological heterogeneity in mantle plumes.
584 *Geochem. Geophys. Geosyst*, *12*(11), doi:10.1029/2011GC003748.
585 Sim, S. J., Spiegelman, M., Stegman, D. R., & Wilson, C. R. (2018). Melt focusing at
586 mid ocean ridges. *Abstract DI43C-0045 presented at 2018 Fall Meeting, AGU,*
587 *Washington, DC. 10-14 Dec.*
588 Smith, W. H. F., & Marks, K. M. (2014). Seafloor in the Malaysia Airlines Flight MH370
589 Search Area. *Eos*, *95*(21), 173–180.
590 Sparks, D. W., & Parmentier, E. M. (1991). Melt extraction from the mantle beneath
591 spreading centers. *Earth Planet. Sci. Lett.,* 105, 368–377.
592 Spiegelman, M. (1993a). Physics of melt extraction: theory, implications and
593 applications. *Philos. Trans. R. Soc. Lond. A*, 342, 23–41.
594 Spiegelman, M. (1993b). Flow in deformable porous media . Part 1 Simple analysis. *J.*
595 *Fluid Mech*., 247, 17–38.
596 Spiegelman, M. (1993c). Flow in deformable porous media. Part 2 Numerical analysis -
597 the relationship between shock waves and solitary waves. *J. Fluid Mech.*, *247*,
598 39–63.
599 Tolstoy, M. (2015). Mid-ocean ridge eruptions as a climate valve. *Geophys. Res. Lett.*,
600 *42*, 1346–1351. https://doi.org/10.1002/2014GL063015

Tucholke, B. E., Lin, J., Kleinrock, M. C., Tivey, M. A., Reed, B., & Jaroslow, G. E. (1997). Segmentation and crustal structure of the western Mid-Atlantic Ridge flank, 25°25'–27°10' N and 0–29 m.y. *J. Geophys. Res.*, *102*(B5), 10203–10223.

von Kármán, T. (1948). Progress in the Statistical Theory of Turbulence. *Proc. Nat. Acad. Science*, *34*, 530–539.

Watts, A. B. (2001). *Isostasy and Flexure of the Lithosphere*. Cambridge, UK: Cambridge University Press.

Weatherley, S. M., & Katz, R. F. (2012). Melting and channelized magmatic flow in chemically heterogeneous, upwelling mantle. *Geochem. Geophys. Geosyst.*, *13*(1), 1–23. https://doi.org/10.1029/2011GC003989

Weatherley, S. M., & Katz, R. F. (2016). Melt transport rates in heterogeneous mantle beneath mid-ocean ridges. *Geochimica et Cosmochimica Acta*, *172*, 39–54. https://doi.org/10.1016/j.gca.2015.09.029

White, R. S., McKenzie, D. P., & O'Nions, R. K. (1992). Oceanic crustal thickness from seismic measurements and rare earth element inversions. *J. Geophys. Res*., 97(B13), 19683–19715.

624 **Figures**

625

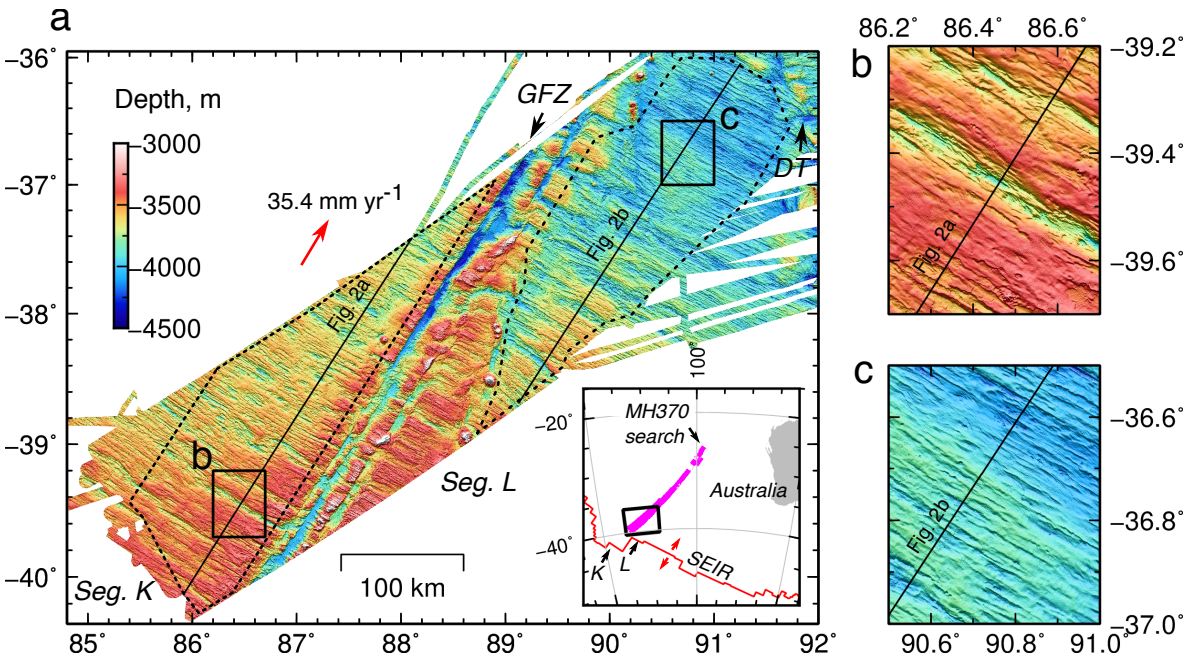

626

627

628

629 **Figure 1.** Multibeam bathymetric data. Inset: Southeast Indian Ridge (SEIR) and
630 spreading vectors (red line/arrows), search area (magenta), study area (black box), and
631 segments K and L. a) Southern portion of MH370 search area, bisected by Geelvinck FZ
632 (GFZ), northern boundary is Diamantina trench (DT); solid black lines are depth profiles
633 shown in Figs. 2a and 2b; dashed black lines are areas selected for profile extraction; red
634 arrow is spreading vector, with half-spreading rate noted. b) and c) Zooms showing
635 seafloor morphology from segments K and L, respectively, highlighting examples of
636 abyssal hills and longer wavelength bathymetric ridges.

637

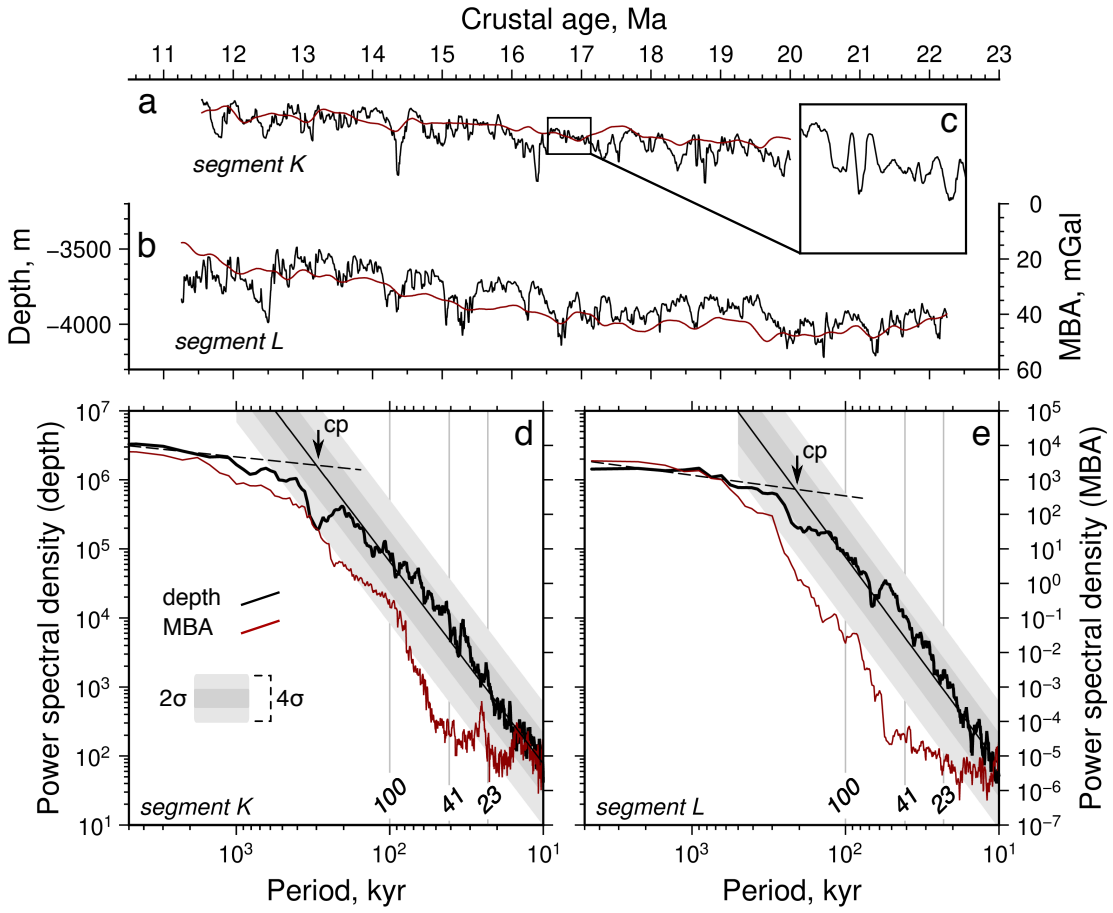

Figure 2. Bathymetric profiles and power spectra. a) and b) Example profiles from segments K and L, respectively; locations shown in Fig. 1. Black/red lines are bathymetry and MBA, respectively; inset (c) shows detailed portion of profile from segment K. (d) and (e) Power spectra calculated from bathymetric and MBA profiles from segment K and L, respectively, without prewhitening; thin solid black line is linear fit to short period 'red' portion of spectra; thin black dashed line is linear fit to long period 'white' portion of spectra; intercept of two fits used to estimate corner period (cp; marked with arrow); dark/light gray bands are 2σ (95% confidence interval) and 4σ bounds for linear fit, respectively. Significant peaks are expected to exceed 4σ bound.

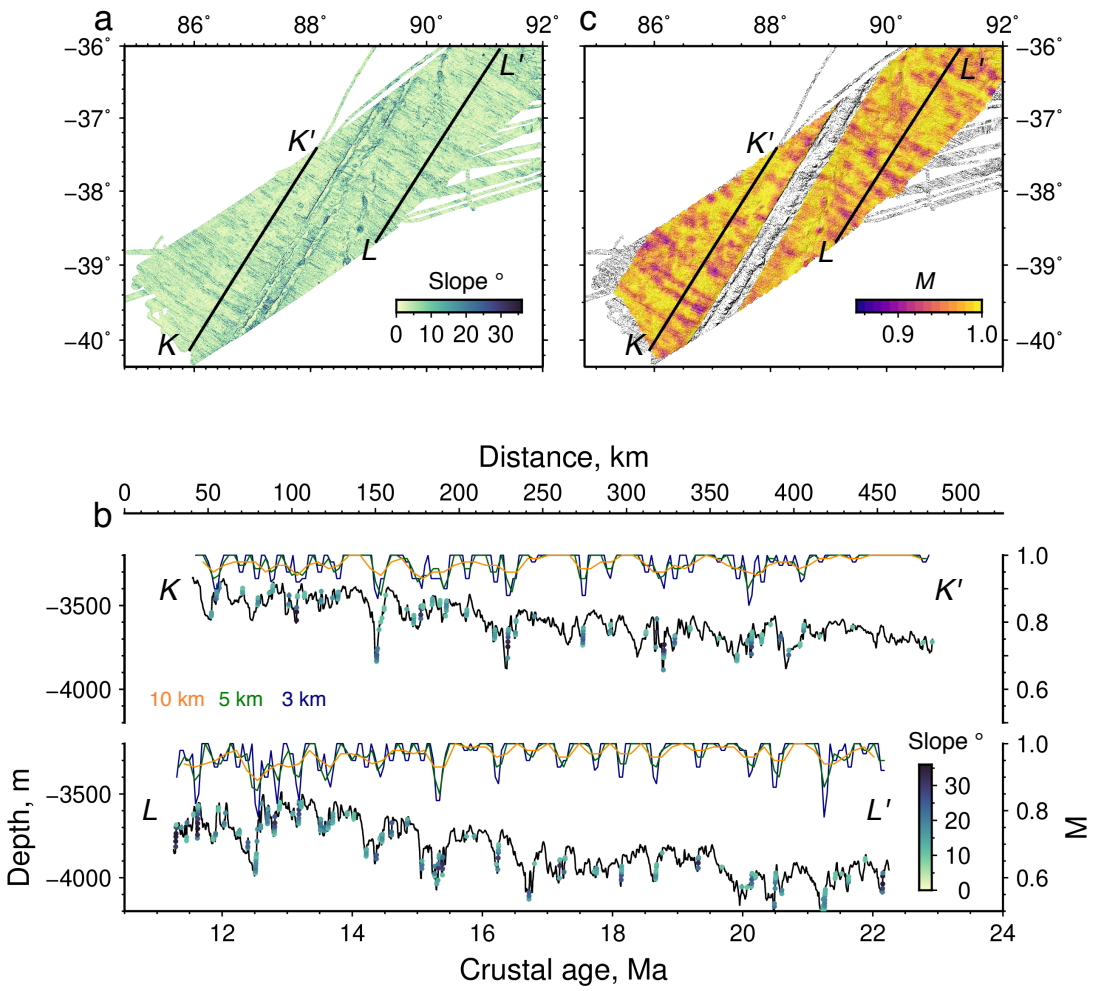

Figure 3. Spatial variations of crustal accretion style. a) Slope map, black lines show examples of profiles used to calculate *M* along plate spreading flowlines. b) Selected bathymetric profiles (black lines), with dots colored by slope where criteria for extensional fault scarps is met; orange/green/blue lines are *M* calculated using 10/5/3 km-long sliding windows, respectively. Profile locations shown in (a). c) Map-view estimate of *M* shaded with bathymetry, obtained by combining adjacent profiles with window length 5 km. Geelvinck FZ excluded from analysis.

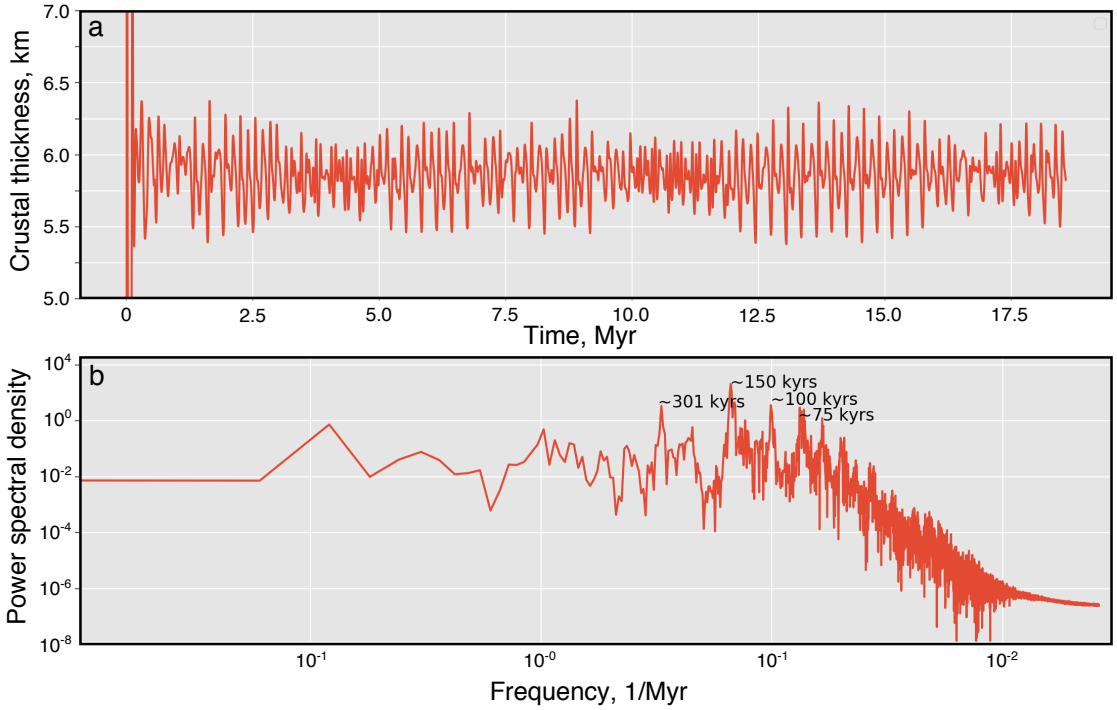

Figure 4. Crustal thickness estimates and resulting spectra derived from 2D two-phase flow modeling for mid-ocean ridge with half spreading rate of 35 mm yr^{-1}. a) Crustal thickness time series model output. b) Power spectral density for time series in a), calculated for time interval starting 2 Myr after initiation of model run to avoid early transient period.